PHYSICAL REVIEW B **108**, 104318 (2023)

Impacts of irradiation-induced nanostructure on phonon linewidths and thermal conductivity in U-Zr alloy

Hao Ma,[1,2,*] Zilong Hua,[3] Amrita Sen,[4] Tiankai Yao,[3] Matthew S. Bryan,[1] Ahmet Alatas,[5] Erika K. Nosal,[6]
Saqeeb Adnan,[6] Enda Xiao,[7] Aaron French,[8] Mukesh Bachhav,[3] Chris A. Marianetti,[9] Marat Khafizov,[6]
Lin Shao,[8] Lingfeng He,[3] Janelle P. Wharry,[4] David H. Hurley,[3] and Michael E. Manley[1,*]

[1]*Materials Science and Technology Division, Oak Ridge National Laboratory, Oak Ridge, Tennessee 37831, USA*
[2]*Department of Thermal Science and Energy Engineering, University of Science and Technology of China, Hefei 230026, Anhui, China*
[3]*Idaho National Laboratory, Idaho Falls, Idaho 83415, USA*
[4]*School of Materials Engineering, Purdue University, West Lafayette, Indiana 47906, USA*
[5]*Advanced Photon Source, Argonne National Laboratory, Argonne, Illinois 60439, USA*
[6]*Department of Mechanical and Aerospace Engineering, The Ohio State University, Columbus, Ohio 43210, USA*
[7]*Department of Chemistry, Columbia University, New York 10027, USA*
[8]*Department of Nuclear Engineering, Texas A&M University, College Station, Texas 77843, USA*
[9]*Department of Applied Physics and Applied Mathematics, Columbia University, New York 10027, USA*

(Received 5 May 2023; revised 7 July 2023; accepted 14 September 2023; published 27 September 2023)

Ion irradiation can significantly change material properties. Thermal conductivity degradation of reactor fuel is detrimental to safety and efficiency—driving research on how irradiation impacts heat-carrying phonons. Here, we report the measurements of phonon dispersion and lifetimes (inverse linewidths) in freestanding irradiated crystals and reveal the relationship between thermal conductivity and proton irradiation induced nanostructures in $UZr_{2.6}$ using inelastic x-ray scattering, electron microscopy, modulated thermoreflectance, and first-principles calculations. Irradiation results in more significant increases in phonon linewidths and decreased thermal conductivity in the basal plane than that along the c axis, decreasing thermal conductivity anisotropy. Microscopy reveals that this results from irradiation induced nanoprecipitates and metastable phase separation. Surprisingly, irradiation leads to smaller phonon linewidths near some zone boundaries, which we attribute to irradiation induced short-range order.

DOI: 10.1103/PhysRevB.108.104318

I. INTRODUCTION

Ion irradiation of materials can significantly impact material properties including thermal [1,2], chemical [3–5], mechanical [3], tribological [6,7], and structural [8] properties. Intentional ion implantation has been widely used to modify or improve surface properties of materials [3,9,10]. In contrast, unintentional irradiation of materials can cause unexpected damage and deleterious consequences. For example, the thermal conductivity of nuclear fuels inevitably degrades in the reactor environment [11], which is directly tied to reactor safety and performance. Although previous studies have attributed thermal conductivity degradation to irradiation induced nanostructural disorder or defects [1] and accompanying phonon lifetime reduction via modeling [12,13], this awaits confirmation by direct phonon lifetimes, nanostructures, and thermal conductivity measurements. Therefore, deeper insight into the relationship between nanostructural evolution, thermal transport, and phonon properties under irradiation is needed to guide the engineering of thermal properties in such materials.

Uranium-zirconium (U-Zr) alloys are attractive as nuclear fuels for next generation fast reactors. The hexagonal δ-UZr_2 phase exists in a relatively narrow composition window near U-50 wt %Zr (U-50Zr or $UZr_{2.6}$) and is stable at room temperature [14]. Recently, Hua *et al.* [15] measured the intragranular thermal conductivity and diffusivity of $UZr_{2.6}$ at room temperature using a modulated thermoreflectance method and found considerable thermal anisotropy ($\sim$10%) in the hexagonal phase. Yao *et al.* [16,17] observed a spinodal-like phase decomposition in a $UZr_{2.6}$ alloy induced by thermal annealing at 893 K and ion irradiation at 823 K. The intermetallic δ-UZr_2 phase also exhibits chemical disorder; the U and Zr atoms randomly occupy positions $(\frac{1}{3}, \frac{2}{3}, \frac{1}{2})$ and $(\frac{2}{3}, \frac{1}{3}, \frac{1}{2})$ in the hexagonal cell [18]. The total thermal conductivity of $UZr_{2.6}$ consists of electronic thermal conductivity (electrons) and lattice thermal conductivity (phonons) [19]. Previous studies [20–22] have demonstrated that irradiation has little impact on electronic thermal conductivity. However, knowledge of how irradiation induced nanostructural evolution impacts phonons and lattice thermal conductivity in $UZr_{2.6}$ is limited and not much is known about the connections between irradiation, nanostructure, phonons, and thermal conductivity.

The only phonon measurements on highly irradiated samples that we know of were performed on UO_2 thin films by Rennie *et al.* [23] using inelastic x-ray scattering (IXS) and they found that phonon linewidths were substantially broadened after irradiation. However, it is desirable to rule out the substrate effects and directly measure freestanding crystals

---

[*] mhao@ustc.edu.cn; manleyme@ornl.gov

2469-9950/2023/108(10)/104318(7)

without relying on thin film fabrication. In this study, we report IXS measurements on phonon dispersion and linewidths in freestanding pristine and proton-irradiated single crystals. The phonon linewidths in irradiated $UZr_{2.6}$ increase more significantly in the basal plane than along the *c* axis. Surprisingly, the linewidths decrease with irradiation at some *q* points. Structural analysis shows that the increased phonon linewidths are attributed to the formation of plateletlike nanoprecipitates and metastable phase separation, resulting in stronger phonon scatterings. The decreased phonon linewidths are likely attributed to the short-range chemical order induced by irradiation. The phonon properties are consistent with changes observed in the thermal conductivity. Namely, irradiation in $UZr_{2.6}$ leads to suppressed thermal conductivity in the basal plane and a relatively small reduction in thermal conductivity along the *c* axis. Our study provides benchmark data on how irradiation induced nanostructures affect phonon transport and thermal conductivity in nuclear fuels and provides guidance for the future design of materials used under irradiation.

II. MATERIALS

$UZr_{2.6}$ crystals were extracted from a 5 mm diameter rod produced by arc melting depleted U and Zr slugs to yield a final nominal chemical stoichiometry of $UZr_{2.6}$. After repeated arc melting, the as-cast rod was cooled to room temperature and then annealed at 550 °C for 24 h to produce a uniform δ-phase microstructure. The rod was then sliced into 0.5 mm thick disk specimens using a high-speed saw. A series of mechanical polishing steps, including a final polishing step consisting of 24 h vibratory polishing using 0.04 µm colloidal silica, was performed to produce a mirror finish on the disk specimen surfaces. One disk was irradiated with 2 MeV protons at room temperature to 1 displacement per atom (dpa) at the Tandem Pelletron Accelerator at Texas A&M University. Small crystals were prepared by focused ion beam (FIB) milling from both the pristine and irradiated specimen using a Thermo Scientific Quanta 3D FEG dual-beam SEM/FIB at the Electron Microscopy Laboratory (EML) facility at Idaho National Laboratory (INL).

III. INELASTIC X-RAY SCATTERING

For IXS measurements $\sim 50\times 50\times 10\,\mu\mathrm{m}^3$ crystals were welded onto a graphite fiber and sealed under the two Kapton tubes (see Fig. S1 in the Supplemental Material (SM) [24]). Phonon dispersion and lifetimes of pristine and irradiated $UZr_{2.6}$ single crystals were measured at beamline 30ID at the Advanced Photon Source (APS), Argonne National Laboratory [25,26] with 23.7 keV X-rays with an energy resolution of 1.5 meV. Measurements were made in the (002), $(00\bar{2})$, (110), (030), and $(2\bar{1}0)$ Brillouin zones and energy spectra were fit with damped harmonic oscillator (DHO) peaks convoluted with the instrumental energy resolution. Although momentum resolution can play a role in extracting phonon linewidth from inelastic neutron scattering (INS) measurement [27] the momentum resolution in IXS is $\pm 0.035\,\text{Å}^{-1}$ for a 50 mm slit, which is much smaller than that in INS and has trivial influence in phonon linewidths. Phonon dispersion and linewidths of pristine (blue) and irradiated (red) $UZr_{2.6}$ measured at room temperature are summarized in Fig. 1 and all data and fits can be found in Fig. S2 in the SM [24]. The elastic peak was fit with the delta function convoluted with the instrumental energy resolution. However, the fits of some elastic peaks were not good enough and require the addition of a DHO under the elastic peaks to obtain high-quality fits. The extra quasielastic scattering most likely originates with the double encapsulation materials (Kapton and glue) required for safety reasons (see Fig. S1 in the SM [24] for illustration). We have followed the same fitting procedure for all measured data (see Figs. S2 and S3 in the SM [24] for details). Figures 1(a)–1(c) show the measured energy spectra at $\boldsymbol{Q} = [0.2,\ 0,\ 2]$ [transverse acoustic (TA)], $\boldsymbol{Q} = [0,\ 0,\ 2.05]$ [longitudinal acoustic (LA)], and $\boldsymbol{Q} = [0.2,\ -3,\ 0]$ (TA) fitted with a damped harmonic oscillator (DHO) convoluted with the instrument energy resolution of 1.5 meV. The effects of irradiation on phonon linewidths are complicated. Compared to the pristine case, irradiated $UZr_{2.6}$ shows a significantly larger phonon linewidth (broader peak) at $\boldsymbol{Q} = [0.2,\ 0,\ 2]$ [Fig. 1(a)] and similar phonon linewidth at $\boldsymbol{Q} = [0,\ 0,\ 2.05]$ [Fig. 1(b)], but, surprisingly, smaller phonon linewidth (shaper peak) at $\boldsymbol{Q} = [0.2,\ -3,\ 0]$ [Fig. 1(c)]. Measured phonon linewidths along high-symmetry lines are shown in Fig. 1(e). Significantly larger linewidths in irradiated $UZr_{2.6}$ mainly occur in the range of $q = 0.1$–0.3 along the $\Gamma \rightarrow M$ direction (in the basal plane) where phonons contribute the largest portion of thermal conductivity due to the combination of large phonon group velocities and significant density of states [2]. However, less significant linewidth broadening presents along the $\Gamma \rightarrow A$ direction (along the *c* axis). Most interestingly, smaller linewidths in irradiated $UZr_{2.6}$ appear at several *q* points (e.g., TA2 at $q = 0.2$ along the $\Gamma \rightarrow M$ direction) compared to pure $UZr_{2.6}$. Note that the TA2 branch along the $\Gamma \rightarrow K$ direction measured in two different Brillouin zones (see blue and green stars) shows similar phonon energies and linewidths, which demonstrates the consistency of our measurements.

IV. CALCULATIONS

Figure 1(d) shows a comparison of the measured phonon dispersion for pristine (blue) and irradiated (red) $UZr_{2.6}$ with calculated phonon dispersion of UZr_2 (black curves) from density functional theory (DFT). Calculations were made within the generalized gradient approximation (GGA) as formulated by Perdew, Burke, and Ernzerhof (PBE) [28] using the projector augmented wave (PAW) method [29,30], as implemented in the Vienna *ab initio* simulation package (VASP) [31–34]. A plane wave basis with an energy cutoff of 400 eV was employed and the approximate *k*-point spacing is $0.1\,\text{Å}^{-1}$. All *k*-point integrations were done using the tetrahedron method with Blöchl corrections [29]. The DFT energies were converged to within 10^{-6} eV. To simulate the disordered crystal structure, we used the quasirandom structure for UZr_2 determined in Ref. [18], which contains 24 atoms. We did not explore quasirandom structures for $UZr_{2.6}$ to mitigate computational costs. Phonons were computed via finite difference using the lone irreducible derivative approach (LID) [35], and the resulting phonons were unfolded to the primitive unit cell of the ordered structure [36]. For the finite difference calculations, up to five displacement amplitudes were

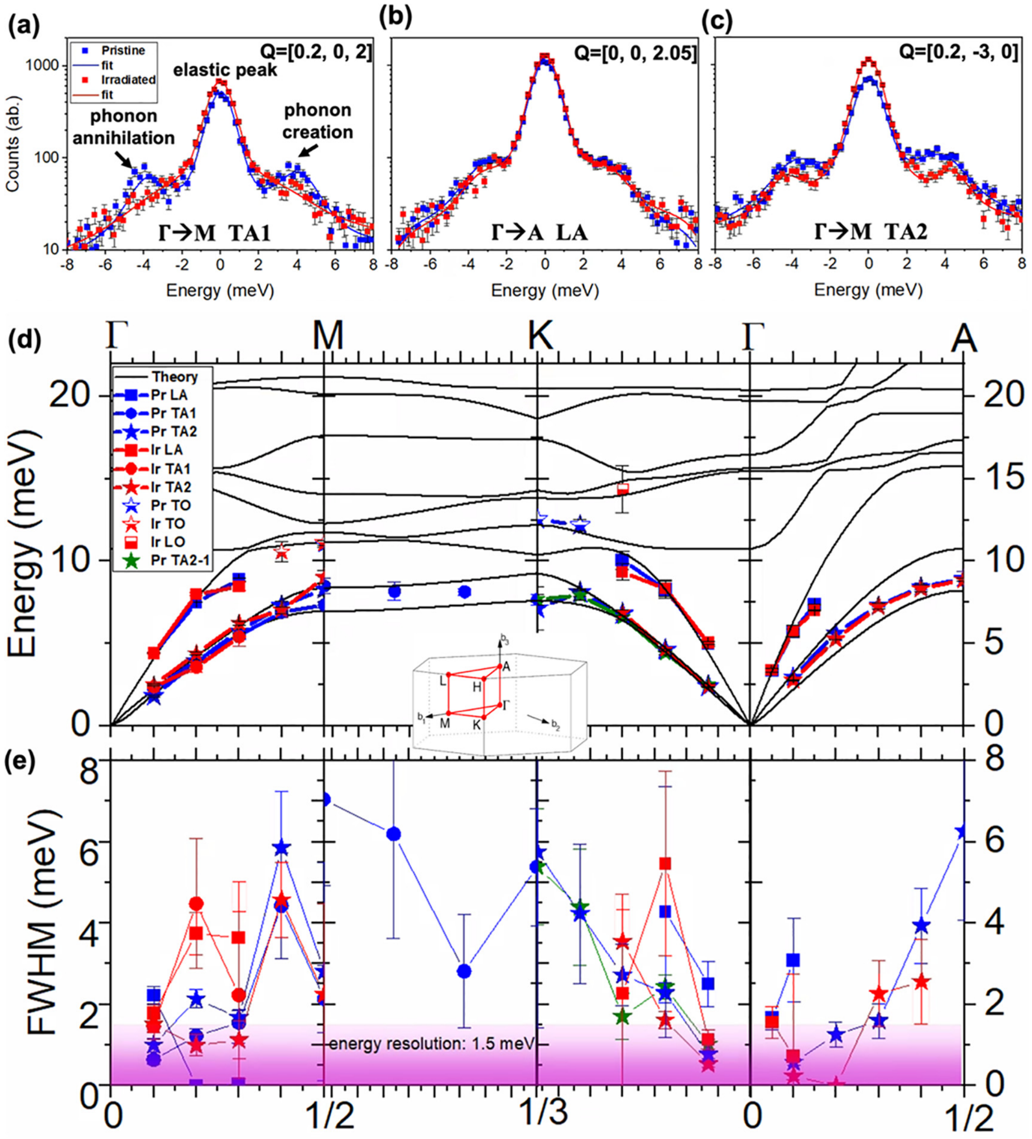

FIG. 1. Phonon dispersion and linewidths of pristine (blue) and irradiated (red) $UZr_{2.6}$ measured using IXS at room temperature. Energy spectra from IXS measurement (squares) of the (a) TA1 at $\boldsymbol{q} = 0.2$ along the $\Gamma \rightarrow M$ direction with $\boldsymbol{Q} = [0.2,\ 0,\ 2]$, (b) LA at $\boldsymbol{q} = 0.05$ along the $\Gamma \rightarrow A$ direction with $\boldsymbol{Q} = [0,\ 0,\ 2.05]$, and (c) TA2 at $\boldsymbol{q} = 0.2$ along the $\Gamma \rightarrow M$ direction with $\boldsymbol{Q} = [0.2,\ -3,\ 0]$. They are characterized by an elastic peak centered at zero energy and inelastic peaks associated with the creation (positive energy) and annihilation (negative energy) of phonons. Blue and red curves represent the best fits using a DHO function convoluted with the instrument resolution function. (d) Measured phonon dispersion and (e) phonon linewidth of pristine and irradiated $UZr_{2.6}$ along high-symmetry directions (see inset for the Brillouin zone). Black curves in (d) denote calculated phonon dispersion of pristine UZr_2 using first principles. Filled and half-filled markers denote acoustic and optical phonons, respectively. The TA2 branch along the $\Gamma \rightarrow K$ direction were measured in two different Brillouin zones: (030), marked by blue stars and (002), marked by green stars. Pink shading in (e) marks the area below instrumental energy resolution (1.5 meV). Note that measured linewidths appearing at zero are too small to resolve given the instrumental energy resolution of 1.5 meV and can only be claimed to be less than ~0.25 meV.

evaluated for a given measurement, such that the discretization error could be extrapolated to zero. The measured phonon dispersion curves of $UZr_{2.6}$ are in general agreement with the calculated phonon dispersion curves of pristine UZr_2 [Fig. 1(d)]. Most importantly, phonon dispersion of irradiated $UZr_{2.6}$ mostly overlaps with that of pristine $UZr_{2.6}$, indicating overall similar phonon group velocities. This is further validated by the acoustic speed of sound extracted from measured phonon dispersion as shown in Table S1 in the Supplemental Material [24].

V. ELECTRON MICROSCOPY

To gain more insights into the irradiation effects, we further investigated the structural changes of pristine and irradiated $UZr_{2.6}$ using scanning tunneling electron microscopy (STEM) on a Thermo Scientific Talos F200X TEM also at EML-INL. The bright-field STEM image in Fig. 2(a) shows an overall uniform structure at the nanoscale in the pristine $UZr_{2.6}$. This is consistent with our previous work where the selected area electron diffraction (SAED) pattern (see Fig. 3(d) in Ref. [37])

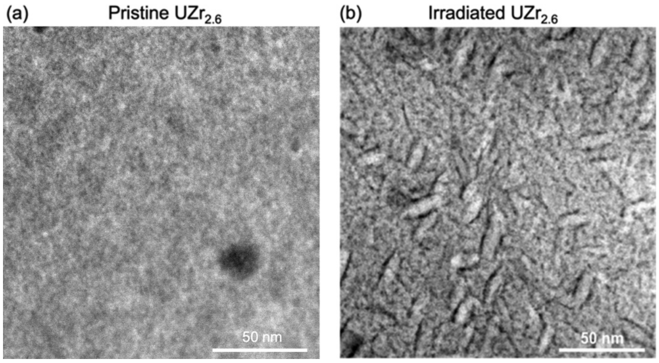

FIG. 2. STEM bright field image of (a) pristine $UZr_{2.6}$, and (b) irradiated $UZr_{2.6}$.

confirms the pristine $UZr_{2.6}$ forms a uniform ordered hexagonal δ-$UZr_{2.6}$ phase. In contrast, significant changes at the nanoscale are observed in irradiated $UZr_{2.6}$. A uniform distribution of plateletlike nanoprecipitates is observed throughout the volume in irradiated $UZr_{2.6}$ in Fig. 2(b). This image is also consistent with previous work but shows more details of the structural features. The SAED pattern in Fig. 6(e) of Ref. [37] shows the crystal structure after irradiation is a combination of α-U, α-Zr, and bcc γ-UZr nanoprecipitates within the δ-UZr_2 matrix. Additionally, the precipitates appear highly aligned along crystallographic directions. The average precipitate length and width are 24.3 ± 6.7 nm and 4.6 ± 1.4 nm, respectively, and the number density within the grain is $1.62 \times 10^{-5}\ \mathrm{nm}^{-3}$. The 1 dpa dose applied in this study is not conducive to equilibrium phase formation and so these observed nanoprecipitate phases may be metastable. More detailed discussion of the crystal structure change due to irradiation can be found in Ref. [37]. These plateletlike nanoprecipitates in irradiated $UZr_{2.6}$ likely serve as phonon scattering centers [12,38,39] and lead to our observed smaller phonon lifetimes (Fig. 1). It is important to note that the irradiation induced plateletlike nanoprecipitates in this study are different from the Zr precipitates in the gamma-phase $UZr_{2.6}$ discussed in a previous study [15]. Here the irradiation induced precipitates are one to two orders of magnitude smaller and consequently are more effective at scattering heat-carrying phonons. Moreover, the length scale of these nanoprecipitates corresponds to $q = 0.1$–0.3 along the $\Gamma \rightarrow M$ direction in the reciprocal space of $UZr_{2.6}$. Therefore, we attribute the observed larger phonon linewidths in this q range in the irradiated $UZr_{2.6}$ to the formation of plateletlike nanoprecipitates and metastable phase separation induced by irradiation. On the other hand, irradiation may reduce the chemical disorder that exists in δ-UZr_2 (namely, the alteration in site occupancy of U and Zr atoms [18]), which has been observed in a proton-irradiated $Al_{0.3}CoFeNi$ alloy [40]. Therefore, smaller phonon linewidths at several q points likely result from the short-range chemical order induced by irradiation.

VI. THERMAL TRANSPORT

The irradiation induced plateletlike nanoprecipitates and metastable phase separation help explain strong phonon scatterings and larger phonon linewidths in $UZr_{2.6}$, which are expected to result in smaller lattice thermal conductivity. Our measured total thermal conductivity for pristine and irradiated $UZr_{2.6}$ polycrystals via the spatial-domain thermoreflectance (SDTR) technique [41] support this argument. In SDTR, a continuous-wave (cw) laser (Coherent OBIS 660 nm) with periodically modulated intensity is used to generate a thermal wave in the sample [42,43], of which the directional heat propagation is probed using another cw laser with constant intensity (Coherent Verdi 532 nm) through the thermoreflectance effect. During our measurements, one laser scans across the other and multiple sets of thermal wave phase data were collected along different scan directions from 0° to 180° in increments of 10°. Both laser beams were focused using a 50× long working distance objective lens (Olympus SLMPlan 50×). The spot size on the sample surface was ∼1 μm for each laser. The power of the heating and probe lasers at the sample surface was measured to be ∼2 and ∼0.3 mW, respectively. More details of this experimental setup can be found in previous studies [41,44]. The SDTR measurements were conducted with the laser modulation frequency of 10–100 kHz. This frequency range was selected by comparing the thermal diffusion length (defined as $L_{\mathrm{th}} = \sqrt{D/\pi f}$, where D is thermal diffusivity and f is modulation frequency of the heating laser) to the damage layer thickness (estimated by using stopping and range of ions in matter (SRIM) simulation) [45,46]. In our measurement, both length scales are in the range of ∼10 μm, which guarantees measurement accuracy. The average grain size of the sample was approximately 200 μm, significantly larger than the thermal diffusion length, thus validating the semi-infinite boundary condition used in the analytical model [45,46]. We determined the orientations of multiple grains with electron backscatter diffraction (EBSD) and measured the effective anisotropic thermal conductivity in each grain. Thermal conductivity in the basal plane (k_a) and along the c axis (k_c) was extracted from the effective anisotropy from the solution of the diffusion equations that take into account grain orientation assuming that specific heat and density are known [47,48]. Unlike previous reports, where samples were aligned along high-symmetry crystallographic orientations, the current thermal wave model includes the rotation of the thermal conductivity tensor to an arbitrary orientation, resulting in a highly anisotropic matrix. An analytical solution to this problem as well as the results of experimental fitting are presented in the Supplemental Material [24]. Multiple measurements were conducted in different grains to improve accuracy and grain size (∼100 μm) is large enough to rule out size effects on thermal conductivity. Depending on the grain orientation, SDTR measurement may have different sensitivity on thermal conductivity along principal directions. Figures 3(a) and 3(b) show one example of selected grain orientations in polycrystalline $UZr_{2.6}$ that provide sufficient sensitivity to thermal conductivity along both principal directions. The measured thermal wave profiles along different directions are depicted as polar plots in Fig. 3(c), which shows the effective thermal conductivity obtained from appropriately adjusting measured slopes along multiple directions. A noticeable anisotropy in pristine $UZr_{2.6}$ (blue) is evident from the aspect ratio of the elliptical shape, while a reduction of thermal conductivity and decrease in anisotropy ratio is observed in the irradiated $UZr_{2.6}$ (red). After analyzing the

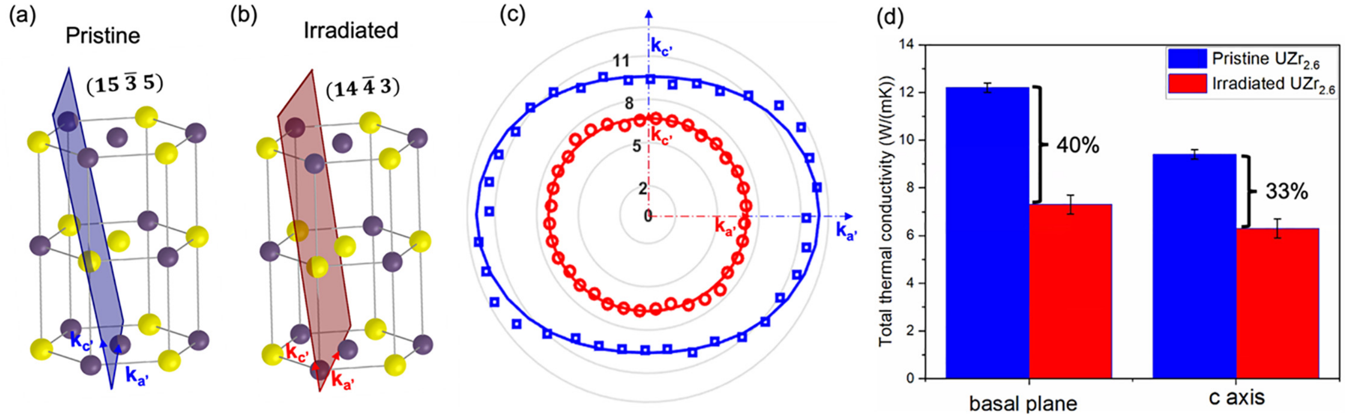

FIG. 3. Summary of thermal conductivity measurements and analysis. Selected grains that provide sufficient sensitivity to both basal plane and c axis thermal conductivities are present in (a) for pristine and (b) for irradiated $UZr_{2.6}$. $k_{a'}$ and $k_{c'}$ are thermal conductivities along the principle directions (a' and c' axis) in the selected grain. (c) Scan direction dependent effective thermal conductivity for both samples show noticeable anisotropy in pristine $UZr_{2.6}$ (blue) and thermal conductivity and anisotropy reduction in irradiated $UZr_{2.6}$ (red). (d) The total thermal conductivity in the basal plane (k_a) and along the c axis (k_c) of the pristine (blue) and irradiated (red) $UZr_{2.6}$ by the SDTR technique and the details on how to extract k_a and k_c from $k_{a'}$ and $k_{c'}$ can be found in the Supplemental Material [24].

thermal wave profile using the heat diffusion equation (see details in the SM [24]), we determine the total thermal conductivity in the basal plane (k_a) and along the c axis (k_c) of pristine $UZr_{2.6}$ [see Fig. 3(d)] are $12.2 \pm 0.2\,\mathrm{W/(mK)}$ and $9.4 \pm 0.2\,\mathrm{W/(mK)}$, an anisotropy ratio of ~1.30. In contrast, k_a and k_c of irradiated $UZr_{2.6}$ are $7.3 \pm 0.4\,\mathrm{W/(mK)}$ and $6.3 \pm 0.4\,\mathrm{W/(mK)}$, a smaller anisotropy ratio of just ~1.16. In addition, the thermal conductivity reduction is ~40% in the basal plane and ~33% along the c axis due to irradiation. This more significant thermal conductivity reduction in the basal plane than along the c axis is consistent with the more pronounced phonon linewidth broadening along the $\Gamma \rightarrow M$ direction as shown in Fig. 2(e).

VII. CONCLUSION

In summary, we performed inelastic x-ray scattering measurements of phonon dispersion and linewidths for pristine and proton-irradiated $UZr_{2.6}$ single crystals at room temperature. We find that irradiation induced formation of plateletlike nanoprecipitates and metastable phase separation in hexagonal $UZr_{2.6}$ led to trivial changes in phonon group velocities but a complicated change in phonon linewidths. Specifically, plateletlike nanoprecipitates result in more significant phonon scatterings and further phonon linewidth broadening in the basal plane compared to along the c axis. Smaller linewidths at some q points likely result from the short-range chemical order induced by irradiation. These are further supported by our measured thermal conductivity. Consistently, a slightly larger reduction in thermal conductivity in the basal plane than along the c axis is observed in irradiated $UZr_{2.6}$ compared to pristine $UZr_{2.6}$. Our study provides deep insights into the relationship between irradiated nanostructures, phonons, and thermal conductivity. The irradiation induced reduction in thermal conductivity anisotropy can guide the future engineering of irradiated materials for energy applications.

The Department of Energy will provide public access to these results of federally sponsored research in accordance with the DOE Public Access Plan [49].

ACKNOWLEDGMENTS

H.M., Z.H., A.S., T.Y., M.S.B., E.K.N., S.A., E.X., C.A.M., M.K., L.H., J.W., D.H.H., and M.E.M. were supported by the Center for Thermal Energy Transport under Irradiation, an Energy Frontier Research Center funded by the U.S. Department of Energy (DOE), Office of Science, United States, Office of Basic Energy Sciences. We would like to acknowledge the U.S. Department of Energy, Office of Nuclear Energy under DOE Idaho Operations Office Contract No. DE-AC07-05ID14517, as part of the Nuclear Science User Facility experiments. This research used resources of the Advanced Photon Source, a U.S. Department of Energy (DOE) Office of Science user facility operated for the DOE Office of Science by Argonne National Laboratory under Contract No. DE-AC02-06CH11357. H.M. also thanks the funding support from University of Science and Technology of China Startup Program (Award No. KY2090000117). This research used resources of the National Energy Research Scientific Computing Center, a DOE Office of Science User Facility supported by the Office of Science of the U.S. Department of Energy under Contract No. DE-AC02-05CH11231.

This work has been supported by UT-Battelle, LLC under Contract No. DE-AC05-00OR22725 with the U.S. Department of Energy. The United States Government retains and the publisher, by accepting the article for publication, acknowledges that the United States Government retains a nonexclusive, paid-up, irrevocable, worldwide license to publish or reproduce the published form of this manuscript, or allow others to do so, for U.S. Government purposes.

[1] T. W. Pfeifer, J. A. Tomko, E. Hoglund, E. A. Scott, K. Hattar, K. Huynh, M. Liao, M. Goorsky, and P. E. Hopkins, Measuring sub-surface spatially varying thermal conductivity of silicon implanted with krypton, J. Appl. Phys. **132**, 075112 (2022).

[2] D. H. Hurley, A. El-Azab, M. S. Bryan, M. W. D. Cooper, C. A. Dennett, K. Gofryk, L. He, M. Khafizov, G. H. Lander, M. E. Manley, J. M. Mann, C. A. Marianetti, K. Rickert, F. A. Selim, M. R. Tonks, and J. P. Wharry, Thermal energy transport in oxide nuclear fuel, Chem. Rev. **122**, 3711 (2021).

[3] W. Ensinger, Modification of mechanical and chemical surface properties of metals by plasma immersion ion implantation, Surf. Coat. Technol. **100-101**, 341 (1998).

[4] G. Wolf, Modification of chemical surface properties by ion beam assisted deposition, Nucl. Instrum. Methods Phys. Res. Sect. B **46**, 369 (1990).

[5] P. Wang, M. Wang, F. Liu, S. Ding, X. Wang, G. Du, J. Liu, P. Apel, P. Kluth, C. Trautmann, and Y. Wang, Ultrafast ion sieving using nanoporous polymeric membranes, Nat. Commun. **9**, 569 (2018).

[6] A. Turos, J. Jagielski, A. Piątkowska, D. Bieliński, L. Ślusarski, and N. K. Madi, Ion beam modification of surface properties of polyethylene, Vacuum **70**, 201 (2003).

[7] H. Dong and T. Bell, State-of-the-art overview: Ion beam surface modification of polymers towards improving tribological properties, Surf. Coat. Technol. **111**, 29 (1999).

[8] V. Švorčík, V. Rybka, V. Hnatowicz, L. Bačáková, V. Lisá, and F. Kocourek, Surface properties and biocompatibility of ion-implanted polymers, J. Mater. Chem. **5**, 27 (1995).

[9] T. Cremer, M. Killian, J. M. Gottfried, N. Paape, P. Wasserscheid, F. Maier, and H. P. Steinrück, Physical vapor deposition of [EMIM][Tf2N]: A new approach to the modification of surface properties with ultrathin ionic liquid films, ChemPhysChem **9**, 2185 (2008).

[10] P. Mazzoldi, Ion beam modification of glass surface properties, J. Non-Cryst. Solids **120**, 223 (1990).

[11] T. H. Bauer and J. W. Holland, In-pile measurement of the thermal conductivity of irradiated metallic fuel, Nucl. Technol. **110**, 407 (1995).

[12] C. A. Dennett, W. R. Deskins, M. Khafizov, Z. Hua, A. Khanolkar, K. Bawane, L. Fu, J. M. Mann, C. A. Marianetti, L. He, D. H. Hurley, and A. El-Azab, An integrated experimental and computational investigation of defect and microstructural effects on thermal transport in thorium dioxide, Acta. Mater. **213**, 116934 (2021).

[13] W. R. Deskins, A. Hamed, T. Kumagai, C. A. Dennett, J. Peng, M. Khafizov, D. Hurley, and A. El-Azab, Thermal conductivity of ThO_2: Effect of point defect disorder, J. Appl. Phys. **129**, 075102 (2021).

[14] M. Kurata, in *Comprehensive Nuclear Materials*, edited by R. J. M. Konings (Elsevier, Oxford, 2012), p. 139.

[15] Z. Hua, T. Yao, A. Khanolkar, X. Ding, K. Gofryk, L. He, M. Benson, and D. Hurley, Intragranular thermal transport in U-50Zr, J. Nucl. Mater. **534**, 152145 (2020).

[16] T. Yao, A. Sen, A. Wagner, F. Teng, M. Bachhav, A. EI-Azab, D. Murray, J. Gan, D. H. Hurley, J. P. Wharry, M. T. Benson, and L. He, Understanding spinodal and binodal phase transformations in U-50Zr, Materialia **16**, 101092 (2021).

[17] T. Yao, A. R. Wagner, X. Liu, A. EI-Azab, J. M. Harp, J. Gan, D. H. Hurley, M. T. Benson, and L. He, On spinodal-like phase decomposition in U-50Zr alloy, Materialia **9**, 100592 (2020).

[18] P. S. Ghosh, A. Arya, C. B. Basak, A. K. Poswal, and S. Banerjee, Chemical ordering as a precursor to formation of ordered δ-UZr_2 phase: A theoretical and experimental study, J. Phys.: Condens. Matter **33**, 254003 (2021).

[19] X. Ding, T. Yao, L. Fu, Z. Hua, J. Harp, C. Marianetti, M. Neupane, M. E. Manley, D. Hurley, and K. Gofryk, Magnetic, transport and thermal properties of δ-phase UZr_2, Philos. Mag. Lett. **101**, 1 (2021).

[20] C. J. Meechan, A. Sosin, and J. A. Brinkman, Thermally activated point defect migration in copper, Phys. Rev. **120**, 411 (1960).

[21] A. J. Terricabras, J. Ferrigno, L. Wang, M. Khafizov, A. T. Nelson, and S. J. Zinkle, Thermal conductivity evaluation of ion irradiated Si_3N_4 and ZrN ceramics using spatial domain thermoreflectance, J. Appl. Phys. **132**, 075105 (2022).

[22] C. A. Dennett, D. L. Buller, K. Hattar, and M. P. Short, Real-time thermomechanical property monitoring during ion beam irradiation using in situ transient grating spectroscopy, Nucl. Instrum. Methods Phys. Res. Sect. B **440**, 126 (2019).

[23] S. Rennie, E. L. Bright, J. E. Darnbrough, L. Paolasini, A. Bosak, A. D. Smith, N. Mason, G. H. Lander, and R. Springell, Study of phonons in irradiated epitaxial thin films of UO_2, Phys. Rev. B **97**, 224303 (2018).

[24] See Supplemental Material at http://link.aps.org/supplemental/10.1103/PhysRevB.108.104318 for sample geometry, IXS fitting of raw data, acoustic speed of sound, and Thermal wave profile analysis.

[25] T. S. Toellner, A. Alatas, and A. H. Said, Six-reflection meV-monochromator for synchrotron radiation, J. Synchrotron Radiat. **18**, 605 (2011).

[26] A. H. Said, H. Sinn, T. S. Toellner, E. E. Alp, T. Gog, B. M. Leu, S. Bean, and A. Alatas, High-energy-resolution inelastic x-ray scattering spectrometer at beamline 30-ID of the Advanced Photon Source, J. Synchrotron Radiat. **27**, 827 (2020).

[27] E. Xiao, H. Ma, M. S. Bryan, L. Fu, J. M. Mann, B. Winn, D. L. Abernathy, R. P. Hermann, A. R. Khanolkar, C. A. Dennett, D. H. Hurley, M. E. Manley, and C. A. Marianetti, Validating first-principles phonon lifetimes via inelastic neutron scattering, Phys. Rev. B **106**, 144310 (2022).

[28] J. P. Perdew, K. Burke, and M. Ernzerhof, Generalized gradient Approximation Made Simple, Phys. Rev. Lett. **77**, 3865 (1996).

[29] P. E. Blöchl, O. Jepsen, and O. K. Andersen, Improved tetrahedron method for Brillouin-zone integrations, Phys. Rev. B **49**, 16223 (1994).

[30] G. Kresse and D. Joubert, From ultrasoft pseudopotentials to the projector augmented-wave method, Phys. Rev. B **59**, 1758 (1999).

[31] G. Kresse and J. Hafner, *Ab initio* molecular dynamics for liquid metals, Phys. Rev. B **47**, 558 (1993).

[32] G. Kresse and J. Hafner, *Ab initio* molecular-dynamics simulation of the liquid-metal–amorphous-semiconductor transition in germanium, Phys. Rev. B **49**, 14251 (1994).

[33] G. Kresse and J. Furthmüller, Efficient iterative schemes for *ab initio* total-energy calculations using a plane-wave basis set, Phys. Rev. B **54**, 11169 (1996).

[34] G. Kresse and J. Furthmüller, Efficiency of *ab-initio* total energy calculations for metals and semiconductors using a plane-wave basis set, Comput. Mater. Sci. **6**, 15 (1996).

[35] L. Fu, M. Kornbluth, Z. Cheng, and C. A. Marianetti, Group theoretical approach to computing phonons and their interactions, Phys. Rev. B **100**, 014303 (2019).

[36] P. B. Allen, T. Berlijn, D. A. Casavant, and J. M. Soler, Recovering hidden Bloch character: Unfolding electrons, phonons, and slabs, Phys. Rev. B **87**, 085322 (2013).

[37] A. Sen, M. Bachhav, X. Pu, F. Teng, T. Yao, and J. P. Wharry, Irradiation effects on stability of δ-UZr$_2$ phase in U-50 wt% Zr alloy, J. Nucl. Mater. **576**, 154251 (2023).

[38] L. A. Turk and P. G. Klemens, Phonon scattering by impurity platelet precipitates in diamond, Phys. Rev. B **9**, 4422 (1974).

[39] M. Khafizov, J. Pakarinen, L. He, and D. H. Hurley, Impact of irradiation induced dislocation loops on thermal conductivity in ceramics, J. Am. Ceram. Soc. **102**, 7533 (2019).

[40] S. Dasari, A. Sharma, T. A. Byers, G. A. Glass, S. Srivilliputhur, B. Rout, and R. Banerjee, Proton irradiation induced chemical ordering in an Al$_{0.3}$CoFeNi high entropy alloy, Appl. Phys. Lett. **119**, 161907 (2021).

[41] D. H. Hurley, R. S. Schley, M. Khafizov, and B. L. Wendt, Local measurement of thermal conductivity and diffusivity, Rev. Sci. Instrum. **86**, 123901 (2015).

[42] Z. Hua and H. Ban, Thermal diffusivity measurement of focused-ion-beam fabricated sample using photothermal reflectance technique, Rev. Sci. Instrum. **88**, 054901 (2017).

[43] A. A. Maznev, J. Hartmann, and M. Reichling, Thermal wave propagation in thin films on substrates, J. Appl. Phys. **78**, 5266 (1995).

[44] Z. Hua, H. Ban, M. Khafizov, R. Schley, R. Kennedy, and D. H. Hurley, Spatially localized measurement of thermal conductivity using a hybrid photothermal technique, J. Appl. Phys. **111**, 103505 (2012).

[45] Z. Hua, A. Fleming, and H. Ban, The study of using a multi-layered model to extract thermal property profiles of ion-irradiated materials, Int. J. Heat Mass Transfer **131**, 206 (2019).

[46] M. F. Riyad, V. Chauhan, and M. Khafizov, Implementation of a multilayer model for measurement of thermal conductivity in ion beam irradiated samples using a modulated thermoreflectance approach, J. Nucl. Mater. **509**, 134 (2018).

[47] Y. Z. Wang, D. H. Hurley, E. P. Luther, M. F. Beaux, D. R. Vodnik, R. J. Peterson, B. L. Bennett, I. O. Usov, P. Y. Yuan, X. W. Wang, and M. Khafizov, Characterization of ultralow thermal conductivity in anisotropic pyrolytic carbon coating for thermal management applications, Carbon **129**, 476 (2018).

[48] P. Jiang, X. Qian, X. Li, and R. Yang, Three-dimensional anisotropic thermal conductivity tensor of single crystalline β-Ga$_2$O$_3$, Appl. Phys. Lett. **113**, 232105 (2018).

[49] http://energy.gov/downloads/doe-public-access-plan